Efficient synergy of photocatalysis and adsorption of hexavalent chromium and rhodamine B over Al_4SiC_4/rGO hybrid photocatalyst under visible-light irradiation

Zhi Fang[a], Qun Li[a], Lei Su[b], Junhong Chen[c], Kuo-Chih Chou[a], Xinmei Hou[a,*]

[a] *Collaborative Innovation Center of Steel Technology, University of Science and Technology Beijing, Beijing, 100083, China*
[b] *Research Center for Bioengineering and Sensing Technology, School of Chemistry and Biological Engineering, University of Science and Technology Beijing, Beijing, 100083, China*
[c] *School of Material Science and Technology, University of Science and Technology Beijing, Beijing 100083, China*

ARTICLE INFO

ABSTRACT

A novel visible-light-driven Al_4SiC_4/rGO hybrid photocatalyst was fabricated using carbothermic reduction and hydrothermal methods. The as-prepared samples were characterized using various techniques and different factors during the photocatalytic reaction were well optimized. Compared with the commonly used photocatalysts, e.g. TiO_2 (P25), g-C_3N_4, etc. the Al_4SiC_4/rGO hybrid not only exhibits super photocatalytic activity in the mixed system containing Cr(VI) and rhodamine B (RhB) but also can degrade different kinds of dyes selectively by modifying surface charge. For the degradation mechanism, there are two stages. The first is the high adsorption capacity owing to surface positive charge on Al_4SiC_4. The second is the active species including photo-electron (e^-) and photo-hole (h^+), which can promote the photocatalytic removal of Cr(VI) and RhB, respectively. In addition, rGO can improve the whole photocatalytic performance via rapid separation and transportation of photoinduced carriers. Furthermore, the cyclic and long-term experiments indicate great reusability and stability of the Al_4SiC_4/rGO hybrid.

1. Introduction

With the rapid development of industry and agriculture, water pollution issues are becoming more and more serious owing to the excessive industrial and agricultural contaminations containing a complex range of toxic inorganic heavy metal ions and poisonous organic compounds [1–3]. These inorganic and organic pollutants, including but not limited to cadmium, lead, mercury, chromium, pesticides, fertilizers and organic dyes, are always highly toxic and do harm to the living beings [4,5]. For instance, hexavalent chromium (Cr(VI)) from industrial activities such as tanning, metal finishing, electroplating, steel production, etc. perceives the top priority on account of its higher toxicity and carcinogenicity even at very low concentration [6]. The permissible limit of Cr(VI) in drinking water is 0.05 mg/L [7]. Therefore, various researches have been carried out to remove Cr(VI) from wastewater. One of the most preferred methods is to convert Cr(VI) to Cr(III) [8] by photocatalysis because Cr(III) is much less toxic than Cr(VI).

Since organic pollutants usually coexist with Cr(VI) in wastewater,

it is highly meaningful to reduce Cr(VI) and oxidize organic pollutants simultaneously. The simultaneous reduction of Cr(VI) and oxidation of dye or phenol have been carried out on TiO_2 and ZnO photocatalysts in the past years. Yu et al. [9] employed a TiO_2-boron doped diamond (TiO_2-BDD) heterojunction to simultaneously oxidize reactive yellow 15 (RY15) and reduce Cr(VI) under UV illumination. Wang et al. [10] investigated the synergistic photosensitized removal of Cr(VI) and RhB dye on amorphous TiO_2. Zhen et al. [11] synthesized porous ZnO nanoplates with a high photocatalytic activity toward the photoreduction of Cr(VI) in the presence of phenol. Nonetheless, TiO_2 and ZnO, etc. can only respond to the UV irradiation accounting for about 4% of the solar energy. Nowadays, significant attention has been given to develop semiconductor-based heterostructures and composite systems for visible-light-driven light harvesting systems [12].

It has been reported that Al_4SiC_4 as a new wide band gap (2.5 eV) semiconductor material [13,14] exhibits unique structures and properties such as outstanding electrical conductivities, electrical resistivity and physicochemical properties [15]. In our recent work, it has been adopted as a sensor for the effective determination of heavy metal ion

* Corresponding author.
  E-mail address: houxinmeiustb@ustb.edu.cn (X. Hou).

$(Cu^{2+}, Cd^{2+}, Pb^{2+})$ [16,17]. To expand the application of Al_4SiC_4 as a new kind of photocatalyst, it is expected to combine with other materials such as electrons accepter or hole accepter to suppress the recombination rate of electron-hole pairs and improve the photocatalytic performance. Reducing graphene oxide (rGO), an excellent electrons accepter [18–21], has been considered as a promising method to improve photocatalytic performance due to its flexible layered feature, chemical inertness, excellent conductivity and high specific surface area [22].

In this work, Al_4SiC_4 in combination with rGO are applied as the photocatalyst for the first time in the simultaneous reduction of Cr(VI) and oxidation of rhodamine B (RhB). To further enhance the photocatalytic performance, surface modification is also adopted, which can remove different kinds of dyes selectively. Compared with the results reported in the literatures, Al_4SiC_4/rGO hybrid photocatalyst exhibits super photocatalytic activity.

2. Experiment section

2.1. Preparation of Al4SiC4 and Al4SiC4/rGO

In this work, all reagents, as analytical reagent grade, were purchased from Sinopharm Chemical Reagent Co., Ltd., Beijing China and used without further purification. Al_4SiC_4 was synthesized using commercial alumina (Al_2O_3, ≥ 98.1 mass%), silica (SiO_2, ≥ 98.8 mass%) and natural graphite (C, ≥ 99.0 mass%) as raw materials in a molar ratio of Al_2O_3: SiO_2: C of 2: 1: 12. The mixtures were ball milled for 24 h with ethanol and dried at 80 °C for 24 h. The obtained mixtures were then pressed into a cylinder under a pressure of 30 MPa and calcined at 1300 °C for 4 h in a tube furnace in flowing high purity argon. The yellow powder was obtained after the furnace was cooled to room temperature. Finally, the powder was ball-milled with ethanol for 4 h for further experiments.

The Al_4SiC_4/rGO hybrid was synthesized by a one-step hydrothermal method in an ethanol water solvent. A certain amount of dried graphene oxide (GO), i.e. 1.5, 4.5, 7.5 and 10.5 mg was dispersed in 60 mL deionized water and 20 mL ethanol under ultrasonication for 60 min. Then 300 mg Al_4SiC_4 powder was added in above GO suspension. The dispersion was sonicated for 30 min and further magnetically stirred for 30 min. This above operation was repeated twice to ensure the suspension to become more uniform. The suspension was then transferred into a 100 mL-Teflon-lined stainless-steel autoclave and heated at 120 °C for 180 min. During the hydrothermal process, GO was reduced to rGO by ethanol as the active agent and Al_4SiC_4 particles were dispersedly attached on the surface of rGO owing to its higher surface area. After being cooled to room temperature, the suspension was centrifuged and dried in an oven at 60 °C for 12 h. Finally, the Al_4SiC_4/rGO hybrids with different rGO contents i.e. 0.5 mass%, 1.5 mass%, 2.5 mass%, 3.5 mass% were obtain.

2.2. Characterization

The phase and structure of all samples were characterized using X-ray diffraction (XRD) analysis on a PW1710 in diffractometer with Cu Kα radiation under operation conditions of 40 KV and 20 mA. The morphology was examined by a field emission scanning electron microscopy (FE-SEM) on a JSM-6701F. Microstructure of Al_4SiC_4 was performed by transmission electron microscopy (TEM), high-resolution transmission electron microscopy (HRTEM) and selected area electron diffraction (SAED) on a JEM-2010 HR. Surface electronic states of Al_4SiC_4 and Al_4SiC_4/rGO were determined by X-ray photoelectron spectra (XPS) using a Thermo Escalab 250Xi with a monochromatic Al Kα source. All blinding energies were referred to the C 1s peak at 284.80 eV of the surface adventitious carbon and revised. The absorption edges and band gaps of all samples were detected by a UV–vis spectrophotometer. Ultraviolet photoelectron spectroscopy (UPS) was

performed with a monochromatic He I light source (21.2 eV) and a VG Scienta R4000 analyzer to obtain the position of valance band maximum (VBM). A sample bias of -5 V was applied to observe the secondary electron cutoff (SEC). The work function (ϕ) can be determined by the difference between the photon energy and the binding energy of the secondary cutoff edge. Zeta potentials were measured by "Malvern Zetasizer Nano ZS" to analyze the surface charge and dispersibility of samples. Photo-luminescence (PL) spectra of samples with an excitation wavelength at 365 nm were carried out to evaluate recombination of photoinduced charge carries.

2.3. Photoelectrochemical measurement

Indium tin oxide (ITO) glass was ultrasonic washed successively using acetone and ethanol for 10 min. It was then cleaned by deionized water and dried as the substrate. A suspension by mixing Al_4SiC_4/rGO power, polyvinylidene fluoride (PVDF) with the mass ratio of 8:2 in N-methyl-2-pyrrolidone (NMP) was coated on ITO glass with a thin coating of 10×10 mm^2. Finally, the ITO glass was dried at 90 °C for 6 h to evaporate the solvent for the later photoelectrochemical detection as the working electrode.

Photoelectrochemical measurement was performed on the conventional three electrodes setup consisting of a platinum plate as the counter electrode, Ag/AgCl (saturated KCl solution) as the reference electrode, Al_4SiC_4/rGO-ITO as the working electrode and 0.2 mol L^{-1} Na_2SO_4 solution as the electrolyte connected to a CHI 760E electrochemical workstation (Shanghai Chenhua Instrument Co., China). The experiments were carried out under visible light irradiation (≥ 400 nm, 100 mW cm^{-2}) using a 300 W Xe lamp (PLS-SXE300UV, Beijing Perfectlight Co., Ltd.). All working electrodes were backilluminated through the ITO glass. Linear sweep voltammetry (LSV) was measured both in the dark and under light illumination from -0.2 to 0.8 V. The photocurrent *vs.* irradiation time curve ($I - t$) was recorded at 0 V and 0.5 V under dark (20 s) and light (20 s) alternately. Electrochemical impedance spectroscope (EIS) was conducted by applying the AC voltage amplitude of 5 mV at 0 V within a frequency range of 0.001–10^5 Hz. Long-time photocurrent decay curve was also recorded for 10,800 s to analyze the photoelectric stability.

2.4. Photocatalytic reduction of Cr(VI)

The photoreduction experiment was carried out using 100 mL solution of potassium dichromate (10 mg L^{-1} Cr(VI), pH is about 3.0 controlled by HCl), which was mixed with 70 mg catalyst. According to the usual experimental procedure reported in the literatures, the mixture should be stirred in the dark to reach adsorption-desorption equilibrium before conducting the photocatalytic reaction. However, in this work, the Al_4SiC_4/rGO hybrid exhibits a strong adsorption capacity with about 98% removal of Cr(VI) after 120 min in the dark. Therefore, it is meaningless to study the photocatalytic performance after the adsorption-desorption equilibrium. In order to investigate the adsorption and photocatalytic performance separately, two parallel experiments were carried out at the same time to investigate the effective photocatalytic performance. In these two parallel experiments, the same suspensions were stirred simultaneously while one was under dark condition and the other was irradiated with visible light by a 300 W Xe lamp with 400 nm cutoff filter (Light intensity density = ca. 100 mW cm^{-2}). The former represents the adsorption performance and the latter represents the overall removal capacity. Furthermore, 3 mL suspension was sampled at each given time interval and centrifuged to get the clear solution. The Cr(VI) concentration was determined spectrophotometrically at 540 nm via 1,5-diphenylcarbazide method [23]. After the optimal rGO content is confirmed, a series of experiments were conducted to investigate the effect of such parameters as pH, catalytic dosage, initial concentration on the adsorption and photocatalysis. The photocatalyst stability was further evaluated by reusing
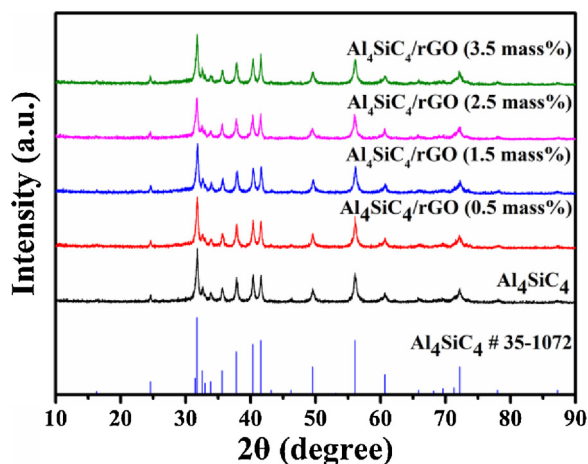
Fig. 1. XRD patterns of Al_4SiC_4 and Al_4SiC_4/rGO hybrids with different rGO contents.

the material in five cycles.

2.5. Simultaneous reduction of Cr(VI) and oxidation of RhB

To investigate the simultaneous reduction of Cr(VI) and oxidation of RhB on Al_4SiC_4/rGO hybrid, 70 mg photocatalyst was added into 100 mL aqueous solution of RhB (10 mg L^{-1}) and Cr(VI) (10 mg L^{-1}). The concentration of Cr(VI) and RhB was determined spectrophotometrically at 540 and 553 nm, respectively. To eliminate the effect of RhB on the Cr(VI), the absorbance of RhB at 540 nm is also recorded and then the Cr(VI) concentration can be determined spectrophotometrically at 540 nm via 1,5-diphenylcarbazide method with subtracting the previous absorbance of RhB at 540 nm. The other reaction conditions and detection methods are kept the same as the above photocatalytic reduction of Cr(VI).

3. Results and discussion

3.1. Structure and morphology

As shown in Fig. 1, all characteristic peaks of the as-synthesized Al_4SiC_4 and Al_4SiC_4/rGO hybrids with different rGO contents are in good agreement with that of hexagonal Al_4SiC_4 (JCPDS Card no. 35-1072). The typical characteristic peaks of rGO, i.e. (002) diffraction peak at 26° and (100) peak at 44.5° [24] in the hybrids are not observed owing to low amount, disordered distribution and relatively low diffraction intensity [25,26].

Fig. 2a shows that ball-milled Al_4SiC_4 particles possess the average particle size of less than 500 nm. However, Al_4SiC_4 particles tend to aggregate. Therefore, rGO is adopted in this work. Fig. 2b–f shows the surface morphology of Al_4SiC_4/rGO hybrids with different rGO contents. In view of the sample with 0.5 mass% rGO addition (Fig. 2b), it is difficult to find rGO sheets. With the content increasing to 1.5 mass%, only a few rGO sheets attached with Al_4SiC_4 particles can be observed (Fig. 2c). Therefore, low rGO content is not enough for the uniform distribution of Al_4SiC_4 particles. The Al_4SiC_4 particles can disperse uniformly on the surface of rGO sheets with the rGO content increasing to 2.5 mass% as shown in Fig. 2d and the EDS elemental mapping confirms the uniform distribution of Al_4SiC_4 in the rGO sheets (Fig. S1). While when the rGO content increases to 3.5 mass%, it leads to the stacking of the rGO sheets with a thickness of up to 1 μm or so as shown in Fig. 2e and f, which weakens the role of rGO as a thin substrate. Therefore, the optimal content of rGO is 2.5 mass% in this work.

To further investigate the microstructure of Al_4SiC_4/rGO (2.5 mass%) hybrid, TEM and HRTEM images were characterized. It is obvious

that the wrinkle-shape structures are rGO (Fig. 3a and b) and there are many well-arranged crystalline lattice fringes corresponding to the (100) and (002) crystal plane of Al_4SiC_4 with the lattice spacing of 0.284 and 1.090 nm, respectively (Fig. 3c–e). The select area electron diffraction (SAED) patterns in the upper illustrations of Fig. 3d–f were viewed along the [0 0 1], [0 1 0] and [1 0 0] zone axis [15,27], respectively. Fig. 3d–e are the optimized crystal structures of Al_4SiC_4 by density functional theory (DFT) viewing along the *c*, *b* and *a* axis, respectively (Fig. S2). Our calculated lattice plane spacings of (100) and (002) are 0.291 and 1.067 nm, which is almost consistent with the experimental data. Detail calculation process is described in supplementary materials. This further proves the Al_4SiC_4 phase in hexagonal structure. Fig. 3f shows the lattice plane from the (100) viewing along *a* axis. The refined lattice constants of Al_4SiC_4 can be obtained from Fig. 3 to be *a* = 3.28 Å, c = 21.80 Å, which are in good agreement with the lattice parameters of Al_4SiC_4 from XRD pattern (JCPDS Card no. 35-1072), with errors of −0.21% and 0.57% respectively.

The surface compositions and functional groups of Al_4SiC_4 and Al_4SiC_4/rGO (2.5 mass%) hybrid were analyzed using XPS as shown in Fig. 4. As for the C 1 s region of the two samples as seen from Fig. 4a and b, the C 1 s region can be divided into five different peaks at 281.2, 282.4, 284.8, 286.3 and 288.8 eV, corresponding to C−Al, C−Si, C−C, C−OH and O−C═O species, respectively [28]. Considering there is no any report on the XPS spectra of Al_4SiC_4 for reference, the peak (282.4 eV) of C−Si specie was determined by the XPS spectrum of SiC [29,30], and the C−Al specie was inferred to be 281.2 eV owing to the weaker binding energy of C−Al than that of C−Si. It is remarkable that there exist many hydroxyl groups (−OH) in pure Al_4SiC_4, which may arise from the surface hydroxylation by ethanol during the process of ball-milling process. The content of each species was calculated semiquantitatively by the peak areas. The content of −OH increases from 16% to 20% after the combination of rGO due to the −OH on the surface of rGO.

Additionally, the O 1 s spectrum of two samples can be deconvoluted into three peaks at approximately 530.3, 531.8 and 533.1 eV, which is assigned to three different oxygen species [12,31–33]. The peak at about 530.3 eV is in good agreement with lattice oxygen (O^{2-}), which may be ascribed to the C−O−C. The main peak at 531.8 eV could be attributed to surface hydroxyl groups, which further proves the presence of −OH on the surface of Al_4SiC_4 particles. Furthermore, the content of −OH increases from 57% to 71% after combining rGO, which is ascribed to the −OH on the surface of rGO. The peak at about 533.1 eV is associated to absorbed O_2^- species on the surface.

3.2. Optical property

The optical properties of Al_4SiC_4 and its hybrids were investigated by UV–vis spectrophotometer. As shown in Fig. 5a, the pure Al_4SiC_4 exhibits strong absorption of visible light. After the combination of rGO, the absorption band edges of the Al_4SiC_4/rGO hybrids occur obvious red shift. The red shift gradually increases with the rGO content increasing, which may arise from the absorption contribution from rGO. In addition, the increase of surface electric charge of the oxides and the modification of the fundamental process of electron-hole formation under irradiation [24,25,34] also contribute to the red shift. Furthermore, the hand gap energy (E_g) values of as-prepared samples were calculated by the following equation [35,36]:

$$\alpha h\nu = A(h\nu - E_g)^{n/2} \tag{1}$$

where *α*, *hν*, *A* and E_g mean the absorption coefficient, photo energy, proportionality constant and band gap, respectively. *n* is equal to 1 or 4, depending on whether the transition is direct or indirect, respectively. According to the previous report, the fundamental absorption of Al_4SiC_4 has a direct transition. Thus, the E_g of the samples were calculated via a plot of the $(\alpha h\nu)^2$ versus *hν*. The value of E_g is obtained by
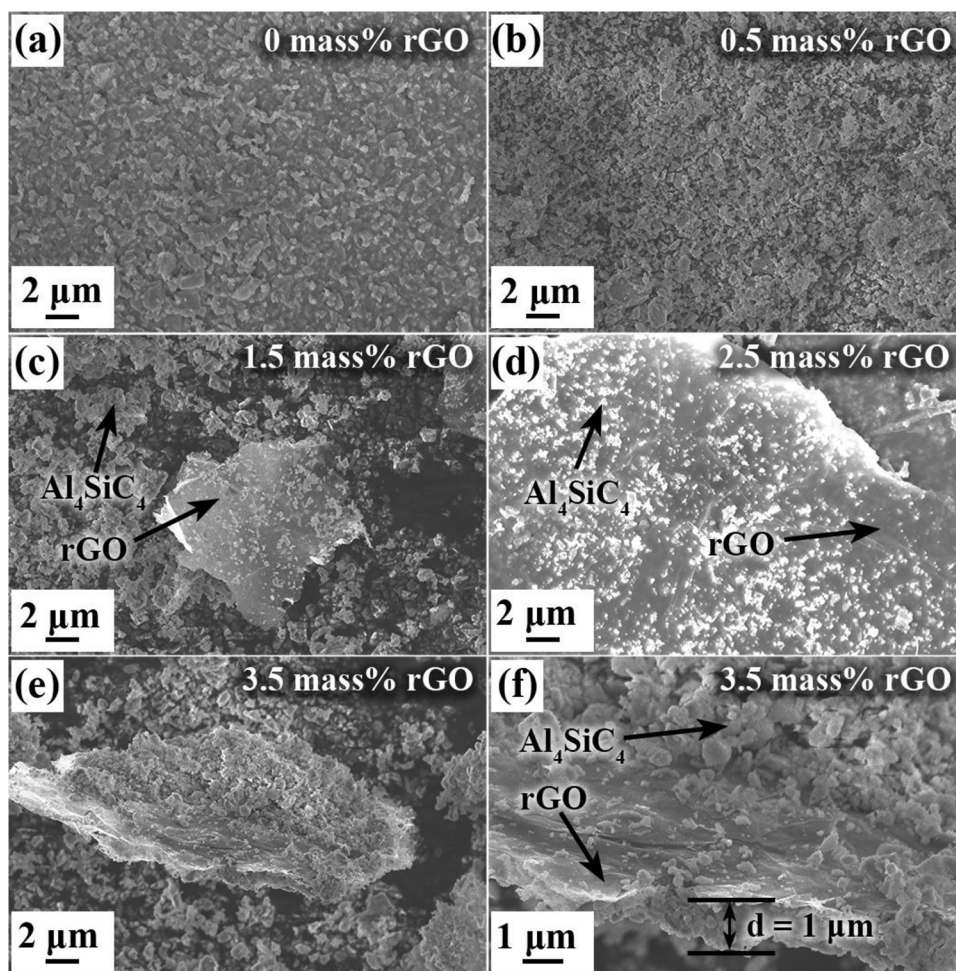
Fig. 2. SEM images of Al$_4$SiC$_4$/rGO hybrids with different rGO contents (a) 0 mass% (b) 0.5 mass%, (c) 1.5 mass%, (d) 2.5 mass%, (e, f) 3.5 mass%.

extrapolating a straight line to the *x* axis (Fig. 5b). The E_g of Al$_4$SiC$_4$ and Al$_4$SiC$_4$/rGO (0.5, 1.5, 2.5 and 3.5 mass%) are estimated to be 2.50, 2.47, 2.45, 2.43 and 2.42 eV, which proves that rGO is beneficial to the photocatalytic property. The light absorption coefficient has also been computed by DFT, as shown in Fig. S3. The calculated band gap is 2.6 eV, which is almost consistent with our experimental band gap (2.5 eV). Fig. 5c and d shows a UPS spectrum for Al$_4$SiC$_4$ sample. From Fig. 5c, the sharp increase in the peak intensity at a binding energy of 18.0 eV is the SEC, so the work function (WF) was calculated by subtracting SEC energy from the excitation energy (*hv*) according to the follow equation: WF = *hv* − SEC (*hv* = 21.2 eV). The obtained WF of Al$_4$SiC$_4$ is 3.2 eV. Then the VBM is determined by taking the intersection of sharp increase line with baseline in valance band spectrum using line extrapolation. As shown in Fig. 5d, the VBM is located at 2.4 eV below E_F, so the energy of VBM and E_F *vs.* vacuum level are −5.6 and −3.2 eV, respectively. Based on the band gap of 2.5 eV, the CBM is located at −3.1 eV. Furthermore, its standard electrode potential of VBM and CBM *vs.* NHE are calculated to be +1.1 V and −1.4 V, respectively, using equation E(eV) = −4.5 − E_{NHE}(V) [37].

3.3. Photoelectrochemical measurement

Photoelectrochemical behavior of Al$_4$SiC$_4$ and Al$_4$SiC$_4$/rGO (2.5 mass%) was measured in 0.2 mol L^{-1} Na$_2$SO$_4$ aqueous solution under darkness or visible-light irradiation (ca. 100 mW/cm^2). As shown in Fig. 6a, LSV, i.e. the *J* − *V* curves are recorded from −0.2 V to 0.8 V under darkness and irradiation. Under visible light irradiation, the current density of Al$_4$SiC$_4$/rGO (2.5 mass%) is larger than that of

Al$_4$SiC$_4$. The *i-t* curves are measured to compare the transient photocurrent responses of Al$_4$SiC$_4$ and the hybrid as shown in Fig. 6b and c. They both possess superior transient photoresponse. At the potential of 0 V (Fig. 6b), the photocurrent curves of the samples have a distinct photocurrent spike, indicating the photocurrent decay. The photocurrent decay can be attributed to the rapid recombination of e^- and h^+. That is exactly the reason for adopting a positive bias potential to promote the separation and transfer of e^- and h^+. The average photocurrent density of Al$_4$SiC$_4$/rGO (2.5 mass%) is about 0.63 μA/cm^2, which is about two times of that of Al$_4$SiC$_4$ (0.24 μA/cm^2). With the addition of a bias potential of 0.5 V, the photocurrent density of Al$_4$SiC$_4$ and Al$_4$SiC$_4$/rGO (2.5 mass%) increased significantly to 1.33 and 6.28 μA/cm^2, respectively (Fig. 6c). At the same time, the decay disappeared, suggesting that the bias potential can promote the separation of photo-generated electron-hole of the photocatalyst and thus prevents the recombination [38,39].

EIS was plotted to further explore the electron transfer efficiency of photoanodes (Fig. 6d). In principle, the arc radius represents the charge transfer resistance at the interface between electrode and solution [40]. By comparison, Al$_4$SiC$_4$/rGO (2.5 mass%) has a much lower interfacial charge transfer resistance under both darkness and irradiation, which proves that rGO can increase the conductivity of the hybrid and improve the photocatalytic performance of Al$_4$SiC$_4$-based hybrid.

Long-time photocurrent decay curves were further recorded at 0.5 V for 10,800 s. As shown in Fig. 6e, the photocurrent responses of Al$_4$SiC$_4$ and Al$_4$SiC$_4$/rGO (2.5 mass%) were both very stable with negligible attenuation after 10,800 s (3 h), which indicates the Al$_4$SiC$_4$ based photocatalysts possess great stability. By contrast, there are many
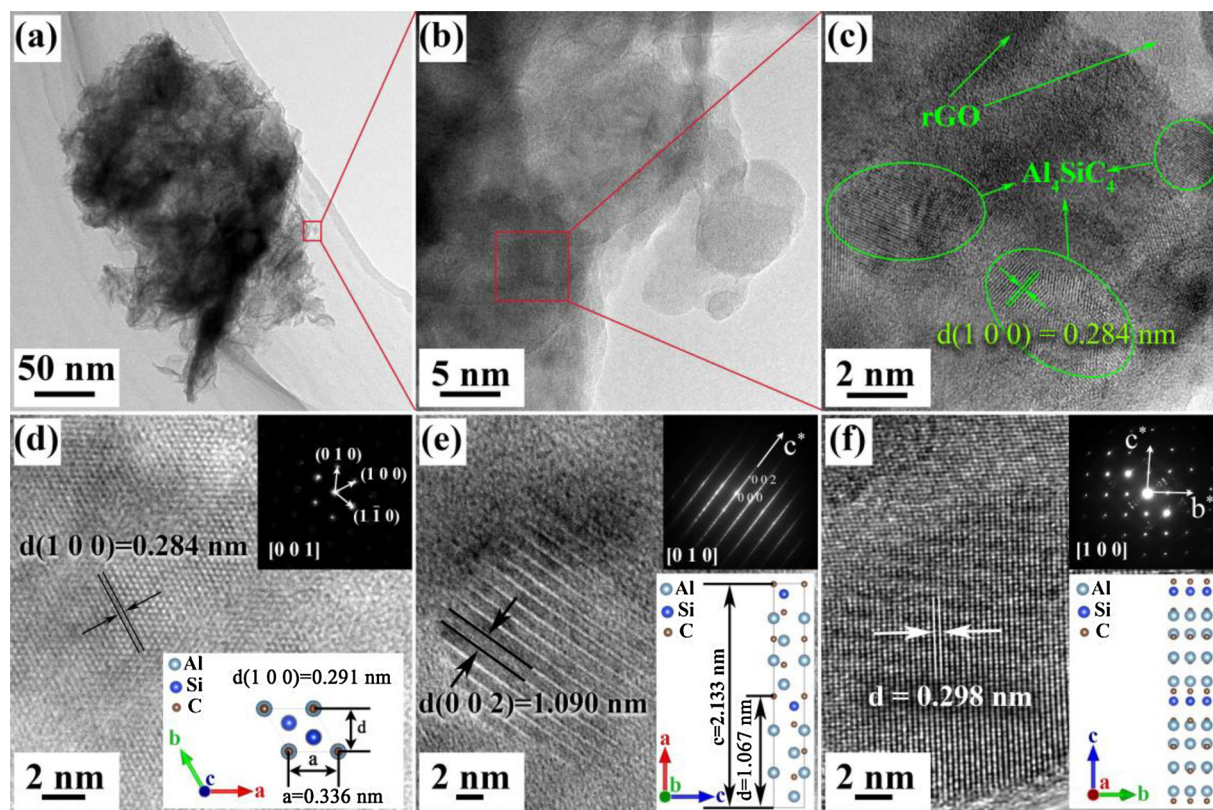
Fig. 3. (a, b, c) TEM and (d, e, f) HRTEM images of Al_4SiC_4/rGO (2.5 mass%). The insets are SAED patterns of Al_4SiC_4 crystal viewed along the [0 0 1], [0 1 0] and [1 0 0] zone axis, and corresponding unit-cell models.

fluctuations in the curve of Al_4SiC_4/rGO (2.5 mass%), which may be caused by the unstable Xe lamp after irradiation for a long time.

3.4. Adsorption and photocatalytic reduction of Cr(VI)

Some important parameters such as rGO content, pH, catalytic dosage and initial concentration on the photoreduction of Cr(VI) have been optimized on the Al_4SiC_4/rGO hybrids shown in the Fig. S4. The optimal content of rGO, value of pH, catalytic dosage and initial concentration of Cr(VI) are 2.5 mass%, 3.0, 0.7 g/L and 10 mg/L, respectively. Fig. 7a shows two parallel experiments of adsorption and photocatalytic reduction of Cr(VI) using Al_4SiC_4/rGO (2.5 mass%) to investigate the adsorption capacity and photocatalytic performance of the hybrids. It exhibits excellent adsorption capacity with about 98% removal of Cr(VI) after 120 min. This is the reason that the photocatalytic reaction was conducted parallelly with adsorption reaction at the same time instead of after the adsorption equilibrium. The maximum adsorption capacity (Q_m) of Cr(VI) is 14 mg/g on Al_4SiC_4/rGO (2.5 mass%), which presents a superiority compared with the previous work (Fig. 7b) [14,23,41–43]. This high adsorption capacity of Al_4SiC_4/rGO (2.5 mass%) hybrid promotes the photocatalytic reduction efficiency of Cr(VI). As shown in Fig. 7a, 98% of Cr(VI) is photo-reduced by Al_4SiC_4/rGO (2.5 mass%) after irradiation for 60 min, exhibiting superior performance compared with the results reported in the literatures (Table 1) [12,24,25,36,44–49]. For example, only 60% of Cr(VI) is reduced in 120 min by commercial TiO_2 (P25) [12]. The reduction rate can reach about 100% by the diatomite-supported TiO_2 while the time is up to 150 min [43]. As for $Bi_{12}GeO_{20}$/g-C_3N_4 composites, although the photocatalytic reduction ratio is almost 100% of Cr(VI) under the visible-light irradiation, the degradation time is longer up to 3 h [36]. The main reason for the high photocatalytic reduction efficiency of Al_4SiC_4/rGO (2.5 mass%) hybrid is possible the hydroxyl groups on the surface of Al_4SiC_4 particles [12], which has been proved

by XPS analyses shown in Fig. 4c. Hydroxyl groups lead to the positive (negative) charges on the Al_4SiC_4 surface in acidic (alkaline) solution (Fig. S5). As a result, the Al_4SiC_4 surface is rich in positive charges in acidic condition. This is also proved by the zeta-potential value as shown in Fig. 7c, where the zeta-potential values of Al_4SiC_4 and Al_4SiC_4/rGO (2.5 mass%) hybrid are as high as 44.46 mV and 47.11 mV, respectively. Due to the characteristic of the opposite charge properties of Cr(VI) (in the form of $Cr_2O_7^{2-}$) and Cr(III) (in the form of Cr^{3+}), the surface positive charges of hybrid are beneficial to the adsorption of Cr(VI) and desorption of Cr(III) [12].

To confirm the reduction of Cr(VI) to Cr(III), we monitored the product of Cr(VI) reduction by analyzing the valence state of Cr that was adsorbed on the photocatalyst. The Al_4SiC_4/rGO (2.5 mass%) photocatalyst was collected after the photocatalytic reaction and the surface composition was characterized by XPS. From the high-resolution spectrum of Cr 2p (Fig. 7d), there are peaks at 577.4 and 587.2 eV ascribable to Cr $2p_{3/2}$ and Cr $2p_{1/2}$ of Cr(III) species ($CrCl_3$) [50]. Since there is no detection of the Cr(VI) peaks (580.8 eV for $2p_{3/2}$ and 589.9 eV for $2p_{1/2}$ of $K_2Cr_2O_7$), it is considered that Cr(VI) is completely converted into Cr(III).

Reusability is an important factor for a catalyst to be considered in practical applications. As shown in Fig. 7e, the reusability of Al_4SiC_4/rGO (2.5 mass%) catalyst was evaluated by the reduction of Cr(VI) via reusing the material in five cycles under visible irradiation. After 60 min of irradiation, 98.3% of Cr(VI) was reduced in the first usage. After the first cycle, the suspension was centrifuged to remove clear liquid and the precipitate was transferred into the fresh Cr(VI) solution to conduct the second cycle, then above steps were repeated for the next cycles. Finally, 98.9%, 99.8%, 98.8% and 96.8% of removal were obtained after 45 min of irradiation in the next four usages, respectively. The Cr(VI) reduction efficiency increased in the 2nd and 3rd run and then decreased slowly. In general, the photo-reduction efficiency is affected by the photoabsorption and photocatalytic activity. The
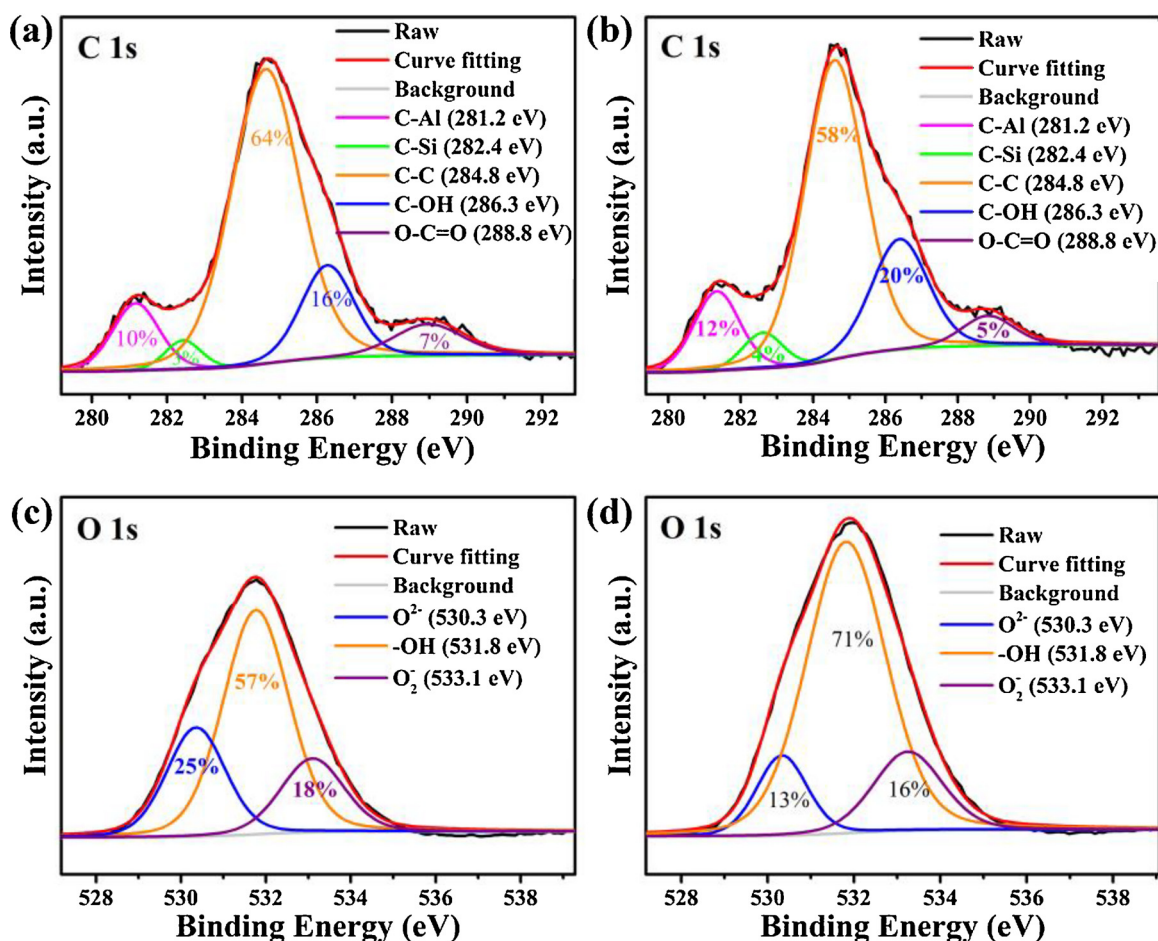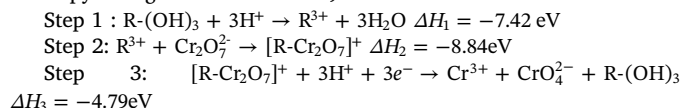
Fig. 4. XPS spectra of (a, c) Al_4SiC_4 and (b, d) Al_4SiC_4/rGO (2.5 mass%): (a, b) C 1 s spectrum, (c, d) O 1 s spectrum.

photoabsorption can be enhanced by improving the despersibility and uniformity of photocatalysts. While the photocatalytic activity declines with the illumination time increasing due to the photocorrosion that is induced by the accumulation of photogenerated holes at the surface of the photocatalysts [51]. In the 2nd and 3rd run, the attenuation of photocatalytic activity can be neglected. Therefore, the photo-reduction efficiency is mainly attributed to the improvement of despersibility and uniformity of photocatalysts. In the 4th and 5th run, the photocatalytic activity declines by 10% or so (Fig. 6e). Its effect cannot be neglected. Therefore, the reduction efficiency decreases. In addition, the Al_4SiC_4/rGO (2.5 mass%) photocatalyst was collected after the photocatalytic reaction. The phase was identified using XRD and it shows all the characteristic peaks correspond to that of Al_4SiC_4, indicating a high stability of this photocatalyst under irradiation (Fig. 7f). Therefore, the Al_4SiC_4/rGO (2.5 mass%) photocatalyst possesses great reusability and stability.

The photoelectrocatalytic (PEC) activity of Al_4SiC_4/rGO (2.5 mass %) photocatalyst was conducted via the PEC reduction of Cr(VI) with the introduction of 0.5 V bias voltage (Fig. S6). Before tuning on the light, the electrode was immersed in Cr(VI) solution for 30 min to achieve adsorption-desorption equilibrium. Result shows a good PEC performance of Al_4SiC_4/rGO (2.5 mass%) photocatalyst.

In view of the reaction mechanism of Cr(VI) reduction, it belongs to solid/liquid heterogeneous catalysis. There are three steps, adsorption on the surface, photo-reduction and surface desorption process [52]. Many researches have proved that the adsorption of Cr(VI) and the desorption of Cr(III) are very important factors in determining the photocatalytic reduction activity of Cr(VI) [12,52]. Nowadays, poor understanding of reaction mechanisms, especially at the molecular

level, is a critical weakness of researches on heterogeneous catalysis [53–55]. In this work, we simulated the adsorption-photoreduction-desorption process of Cr(VI) on the surface of Al_4SiC_4 via DFT for the first time (Fig. 8). We divided the process of reduction of Cr(VI) into three steps as follow (R represents the Al_4SiC_4 surface and ΔH are the enthalpy changes of the reactions):

Step 1 : $R\text{-}(OH)_3 + 3H^+ \rightarrow R^{3+} + 3H_2O$ $\Delta H_1 = -7.42$ eV
Step 2: $R^{3+} + Cr_2O_7^{2-} \rightarrow [R\text{-}Cr_2O_7]^+$ $\Delta H_2 = -8.84$ eV
Step 3: $[R\text{-}Cr_2O_7]^+ + 3H^+ + 3e^- \rightarrow Cr^{3+} + CrO_4^{2-} + R\text{-}(OH)_3$ $\Delta H_3 = -4.79$ eV

In step 1 (Fig. 8a–e), hydroxyl groups ($-OH$) on the surface of Al_4SiC_4 particles can be transformed into $-OH_2^+$ by absorbing the H^+ in acid solution. Then, the $-OH_2^+$ groups are desorbed in the form of neutral H_2O molecules, so the positive charges of $-OH_2^+$ transfer to the surface of Al_4SiC_4. As a result, the Al_4SiC_4 surface is rich in positive charges. The atom relaxation animation of the dissociation of hydroxyls has been simulated via DFT (Supporting Information (SI)-movie01). Besides, hydroxyls can be dissociated regardless of the adsorption site and hydroxyls (OH)-coverage (see SI-movie02 and SI-movie03). The large negative enthalpy change of step 1 indicates the dissociation of hydroxyl groups on Al_4SiC_4 is spontaneous in acidic solution, which is inconsistent with the report of Li et al. [12] where $-OH_2^+$ group can keep stable on the surface of TiO_2. We also simulated the adsorption of H^+ on hydroxyl modified TiO_2 via DFT (SI-movie04). The result proves the Li's report and the disagreement may be attributed to the difference of bond energy between C−O and Ti−O. Isosurfaces of the difference charge density of Al_4SiC_4 surface after $-OH_2^+$ being desorbed in the form of H_2O (Fig. S7b) indicate the breaking of C−O. Electron depletion on Si atom clearly seen in Fig. S7b proves that electron transfers from
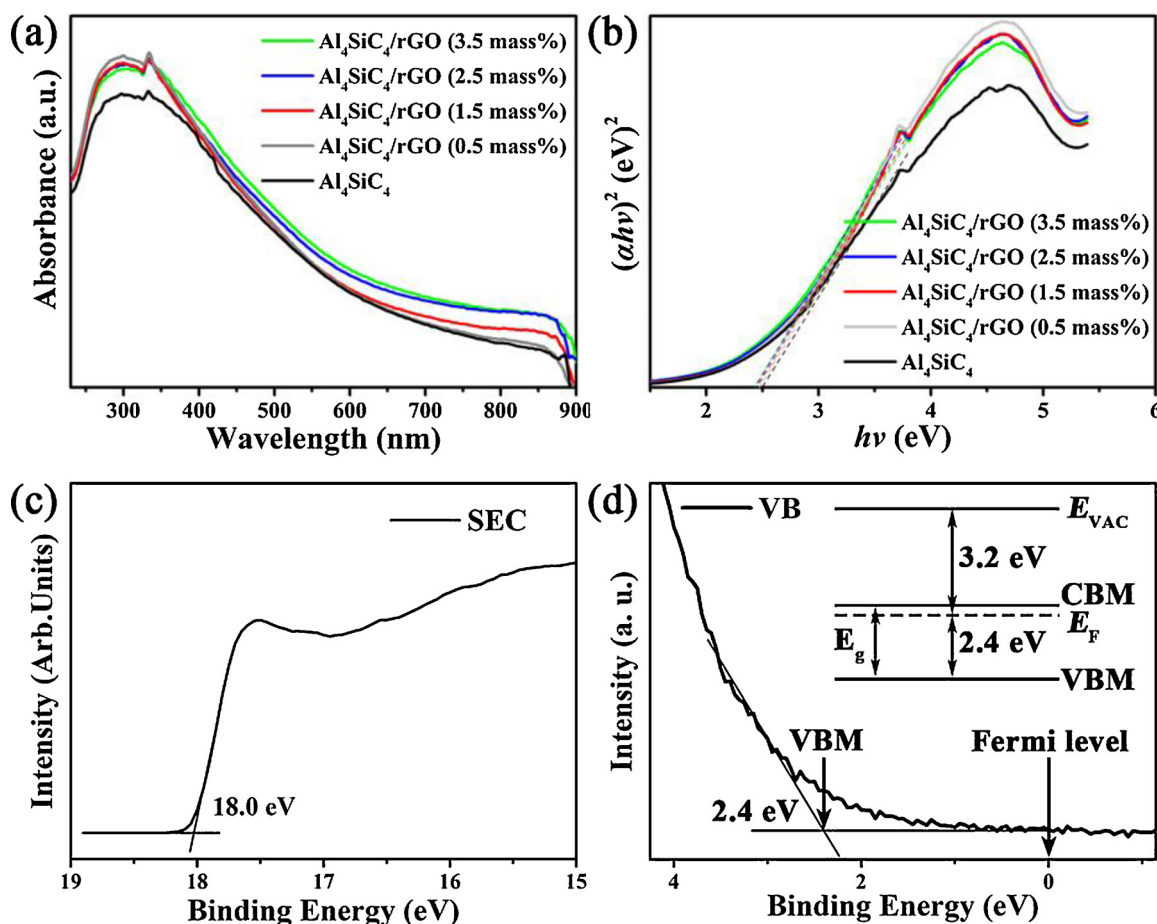
Fig. 5. (a) UV–vis diffuse reflection spectra and (b) plot of the $(\alpha h\nu)^2$ versus $h\nu$ for pure Al_4SiC_4 and Al_4SiC_4/rGO hybrids with different rGO contents. UPS spectrum of (c) the secondary electron cutoff (SEC) and (d) valence-band (VB) region of Al_4SiC_4. The illustration in (d) expresses the relative position of VBM and Fermi level (E_F) to vacuum level (E_{VAC}). The E_F is set to 0 eV.

the Al_4SiC_4 to the adsorbed H^+ and the surface becomes positively charged. Furthermore, in alkaline solution hydroxyl groups lead to the negative charges on the Al_4SiC_4 surface, which is illustrated in Fig. S5b and SI-movie05. Step 2 is the adsorption of Cr(VI) (Fig. 8f–g). $Cr_2O_7^{2-}$ anion is easily adsorbed on the surface of Al_4SiC_4 with positive charge. The adsorption energy of $Cr_2O_7^{2-}$ is -852.93 kJ/mol (-8.84 eV) and the R—O bond lengths are 1.42, 1.71 and 1.73 Å. The high exothermal value and short bond length mean that this step is the chemical adsorption, which is a key factor for the heterogeneous catalysis [54]. The calculated result proves the high adsorption capacity of our catalysts. The atom relaxation animation of Cr(VI) adsorption is shown in SI-movie06. Furthermore, the chemical adsorption can activate adsorbed molecular/ion by electron transfer, exchange or sharing [56] and thus decrease reaction activation energy [57]. The different charge density (Fig. S7c) confirms the charge transfer from Al_4SiC_4 surface to the $Cr_2O_7^{2-}$ ion, so $Cr_2O_7^{2-}$ ion is activated, which benefits the subsequent reduction. In step 3 (Fig. 8h–i), Cr(VI) is reduced to Cr(III) by the catalysis of photo-induced electrons. At the beginning, the photo-induced electrons (e^-) are produced under illumination and then transfer to the surface of Al_4SiC_4. Owing to the strong electron-withdrawing property of Cr(VI), three e^- first transfer to the Cr_1 thought O_1, O_2 and O_3 (Fig. 8g–h). The difference charge density plots reveal that there is a large region of charge accumulation around the Cr_1 atom while no charge change on Cr_2 (Fig. S7c). Therefore, the Cr_1 prefers to be reduced fast. With the e^- transferring to the Cr_1 atom, the Cr_1—O_4 bond is broken and then Cr_1 is reduced to Cr(III). After three H^+ adsorbing on O_1, O_2 and O_3, the Cr_1—O_1, Cr_1—O_2 and Cr_1—O_3 bonds are broken forming Cr^{3+}. Finally, Cr(III) is desorbed from Al_4SiC_4 surface and the

surface of Al_4SiC_4 returns to its original state (Fig. 8a).

3.5. Simultaneous reduction of Cr(VI) and oxidation of RhB

To investigate the photocatalytic performance of Al_4SiC_4/rGO hybrid for simultaneous reduction of Cr(VI) and oxidation of RhB, experiments was conducted on the 100 mL of mixture solution of RhB ($10\,mg\,L^{-1}$) and Cr(VI) ($10\,mg\,L^{-1}$). As shown in Fig. 9, the blank experiment was carried out under irradiation without any catalyst in RhB and Cr(VI) mixture. The red and blue lines represent experiments plotted conducted in single Cr(VI) or RhB solution and the mixture solution, respectively. The other reaction conditions are kept the same, i.e. pH = 3.0, 0.7 mg/L catalyst, $100\,mW/cm^2$. Fig. 9 shows the adsorption and photocatalytic performance of Cr(VI) and RhB in single Cr(VI) solution or mixture solution. As for the photocatalytic removal of Cr(VI) in Fig. 9a, the removal efficiency of Cr(VI) maintains almost unchanged after the addition of RhB. Therefore, the Al_4SiC_4/rGO hybrid is promising to oxidize the RhB dye without degrading reduction of Cr(VI). While the removal efficiency of RhB in mixture solution is lower than that in RhB single solution (Fig. 9b). The main reason is that the RhB is cationic dye [58], producing RhB^+ cation in aqueous solutions. While Al_4SiC_4 has positive charges on the surface at pH = 3.0 (Fig. 7c). Thus Al_4SiC_4 hybrid has a weaker adsorption capacity for RhB in acidic condition owing to the repulsive interaction between positive charges. Hence, RhB prefers to be degraded under alkaline conditions (Fig. S8). Although the adsorption of Cr(VI) and RhB are suppressed by each other, the photocatalysts prefer to adsorb Cr(VI) anions. The simultaneous reduction of Cr(VI) and oxidation of RhB was achieved to be 96%
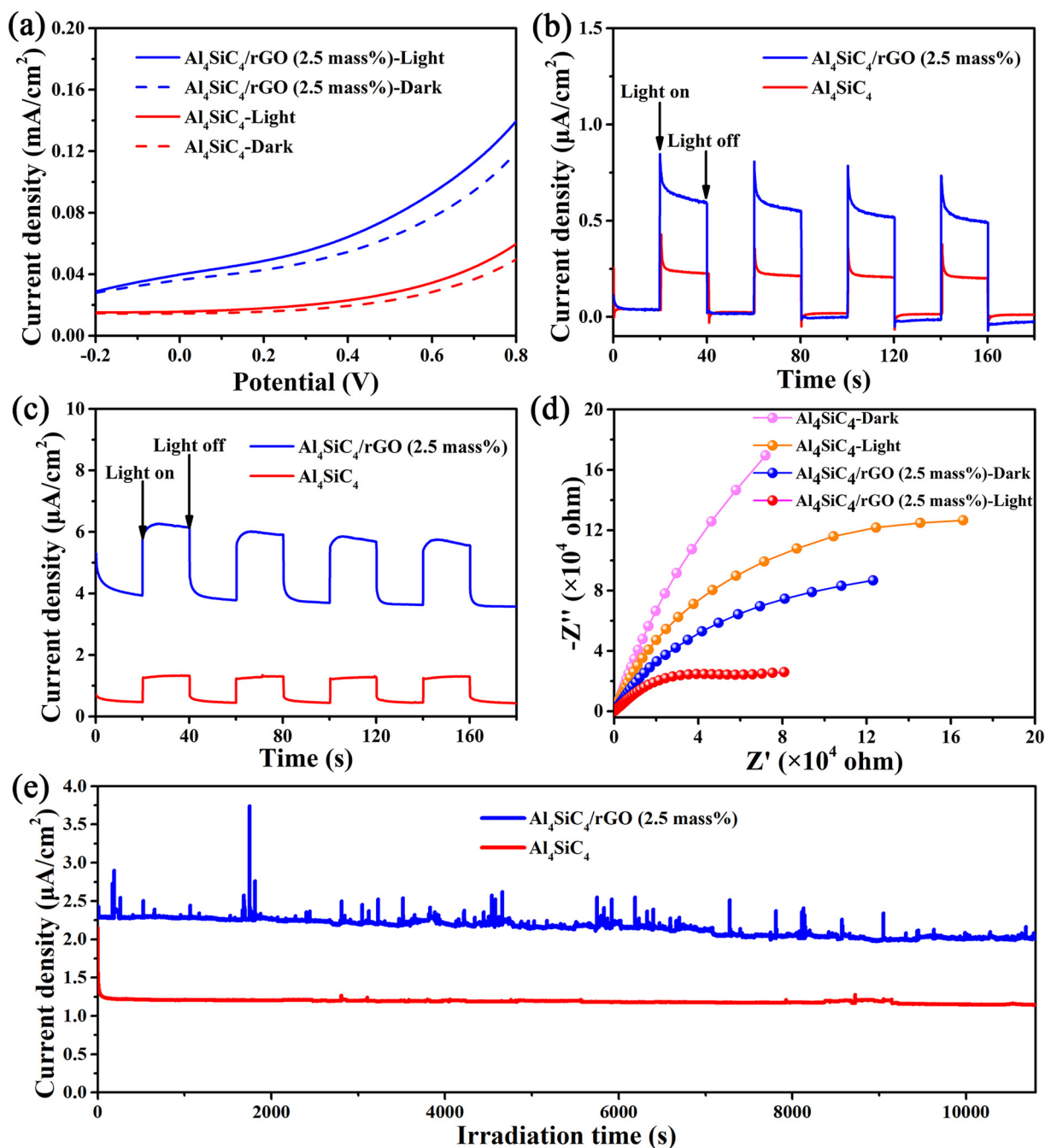
Fig. 6. (a) LSV curves from −0.2 V to 0.8 V, i − t curves at (b) 0 V and (c) 0.5 V, (d) EIS Nyquist spectra at 0 V with the frequency range from 0.001 to 100 kHz and (e) photocurrent decay curves for 10800 s of Al_4SiC_4 and Al_4SiC_4/rGO (2.5 mass%).

of Cr(VI) and 45% of RhB in 60 min. In addition, the hybrid also exhibits high photoelectrocatalytic performance on the simultaneous removal of Cr(VI) and RhB (Fig. S9).

The simultaneous removal of Cr(VI) and other organic pollutants, i.e. methyl orange (MO) over Al_4SiC_4/rGO (2.5% mass%) was also conducted. MO is one of the well-known anionic dyes, producing MO^- anion. It is noteworthy that MO prefers to be degraded under acidic conditions, which is the opposite of the behavior of RhB. It shows 91% of Cr(VI) and 52% of MO were removed under 120 min irradiation (Fig. S10). Considering wastewater always contains more than one kind of dyes, it is of great significance to examine the photocatalytic efficiency of Al_4SiC_4/rGO (2.5 mass%) in the treatment of wastewater that contains different dyes. As shown in Fig. S11, a mixture containing two (MO and reactive red X-3B (RR)) or three (MO, RR and methylene blue

(MB)) kinds of dyes can be efficiently treated over Al_4SiC_4/rGO (2.5 mass%) within 60 min or so. It is further proved that anionic dyes (MO, RR, etc.) and cationic dyes (RhB, MB, etc.) can be degraded efficiently by Al_4SiC_4/rGO (2.5 mass%) photocatalyst under acidic and alkaline conditions, respectively.

3.6. Mechanism of simultaneous reduction of Cr(VI) and oxidation of RhB

The controlled experiments using different radical scavengers were carried out to understand the photocatalytic reaction mechanism. Owing to the fact that $Cr_2O_7^{2-}$ can react with most radical scavengers and Cr(VI) is widely believed to be reduced to Cr(III) by photo-electron of catalyst [59], the scavenging experiments are performed in single RhB solution. The RhB solution with Al_4SiC_4/rGO (2.5 mass%) catalyst

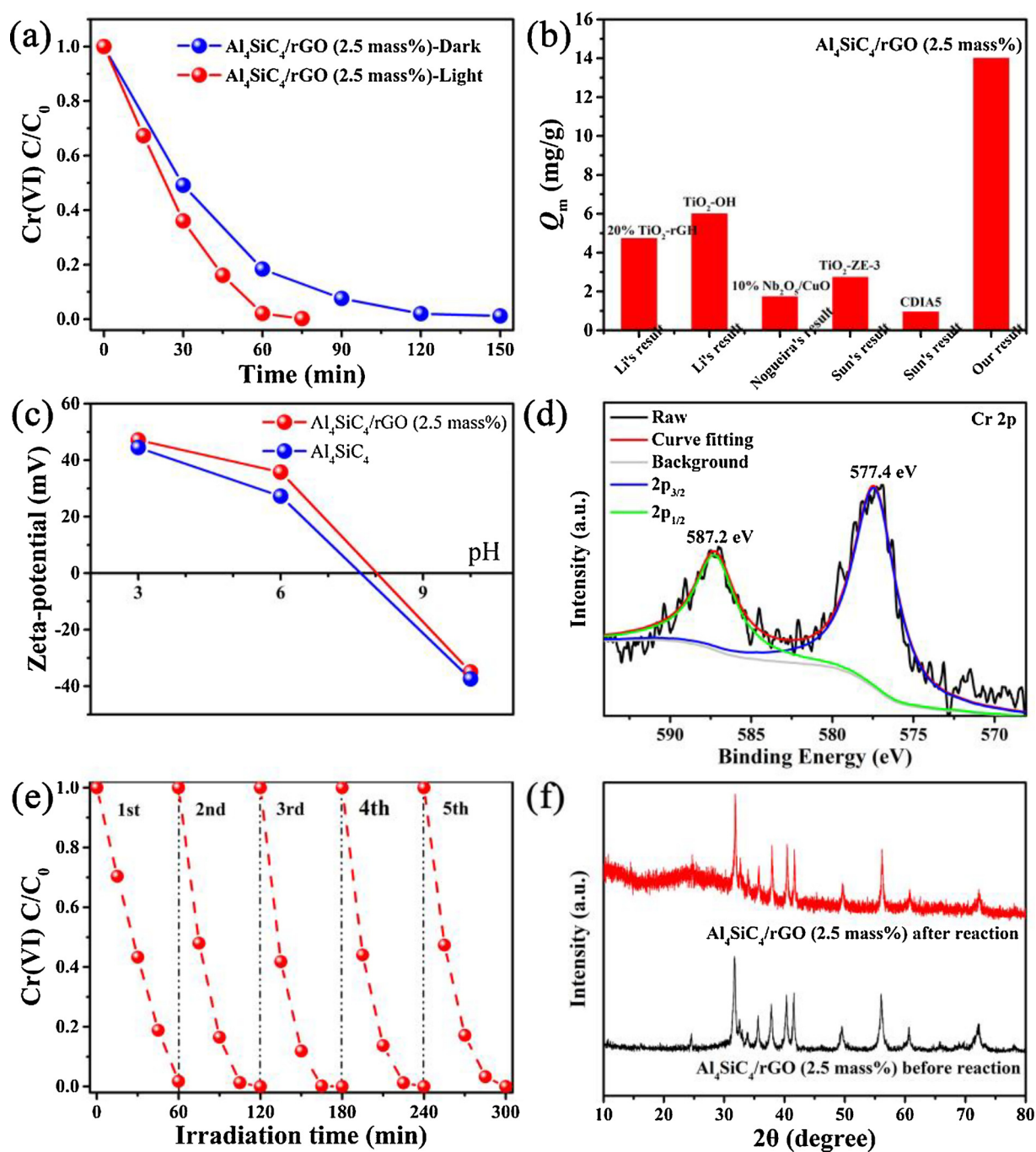**Fig. 7.** (a) Removal of Cr(VI) under darkness and irradiation using Al_4SiC_4/rGO (2.5 mass%) hybrid. (b) Maximum adsorption capacities of Cr(VI) on different photocatalysts. (c) Zeta potentials of pure Al_4SiC_4 and Al_4SiC_4/rGO (2.5 mass%) hybrid. (d) Cr 2p spectrum of Al_4SiC_4/rGO (2.5 mass%) after photocatalytic reaction. (e) Reusability of Al_4SiC_4/rGO (2.5 mass%) photocatalyst in five runs. (f) XRD of Al_4SiC_4/rGO (2.5 mass%) before and after photocatalytic reaction.

was magnetically stirred in dark for 60 min to achieve the adsorption/desorption equilibrium between RhB and catalysts. Then three scavengers were selected [60,61], namely, tert-tutyl alcohol (TBA, hydroxyl radical scavenger), disodium ethylenediaminetetraacetate (EDTA, hole scavenger) and p-benzoquinone (BQ, superoxide scavenger) were added in the RhB solution under irradiation, respectively. The quantities of TBA, EDTA and BQ are 10, 2, 0.15 mM, respectively. The results are shown in Fig. 10a. It is noteworthy that the degradation efficiency was slightly reduced by 13.3% and 10.3% by the injection of scavengers for ·OH (TBA) and ·O_2^- (BQ), respectively, implying that ·OH and ·O_2^- play a little role in this photocatalytic degradation process. However, when the hole quencher (EDTA) was added, the

degradation of RhB was remarkably depressed, indicating hole was the predominant oxidative specie in these reactions.

To acquire the further insight about the interaction between Al_4SiC_4 and rGO, photo-luminescence (PL) spectroscopy of the Al_4SiC_4 hybrids with an excitation wavelength at 365 nm were carried out as shown in Fig. 10b. Strong emission peaks at around 600 nm assigning to the recombination of the electron-holes can be prevented by introducing rGO combined with Al_4SiC_4 particles. After the introduction of rGO, the PL intensity of Al_4SiC_4/rGO hybrids decreases dramatically. It reveals that recombination of photoinduced charge carries is restrained in the Al_4SiC_4/rGO hybrids due to the existence of electron acceptor (rGO). By comparison, the PL intensity of Al_4SiC_4/rGO (2.5 mass%) hybrid is the
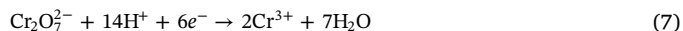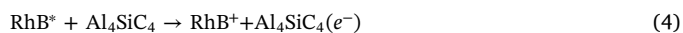
Table 1

The comparison of the removal efficiency of photocatalytic Cr(VI) reduction by different materials reported in the literature with this work.

Systems	pH	Catalyst dosage (g/L)	[Cr (VI)]$_0$ (mg/L)	Time (min)	Removal efficiency (%)	Reference
TiO$_2$ (P25)	3.0	1.0	10	120	60.0	[12]
CdS/RGO-1.5%	–	1.0	10	240	92.0	[24]
ZnO/RGO-1.0%	–	1.0	10	60	96.0	[25]
Bi$_{12}$GeO$_{20}$/g-C$_3$N$_4$	2.5	3.0	10	180	100.0	[36]
Diatomite-supported TiO$_2$	2.1	2.0	10	150	100.0	[43]
5% RGO/ZnO-S1	6.8	0.25	10	80	98.0	[44]
1% BN/BiOCl	2	0.8	10	150	91.7	[45]
TiO$_2$/RGO-0.8%	–	1.0	10	240	91.0	[46]
SPNH-MOSF@SnS$_2$	7	1.0	50	90	99.5	[47]
SnS$_2$/SnO$_2$	5.3	1.0	50	40	99.0	[48]
ZnO-TiO$_2$	3	1.0	20	120	100.0	[49]
Al$_4$SiC$_4$/rGO (2.5 mass %)	3	0.7	10	60	98.0	Our work

smallest, indicating that it is the optimal content to suppress recombination. This is consistent with the tendency of reduction of Cr(VI) (Fig. S4a). It is well known that photocatalytic reaction is mainly influenced by the effective separation and transportation of photoinduced carriers [62]. With the decrease of recombination of photoinduced electron-hole pairs, more electrons will participate in the photocatalytic reduction of Cr(VI) and more holes will be involved in the photocatalytic oxidation of RhB.

Based on the above results, the photocatalytic mechanism of simultaneous reduction of Cr(VI) and oxidation of RhB is proposed as shown in Eqs. (2)–(7) and Fig. 11. The Al$_4$SiC$_4$ semiconductor can be activated by visible-light owing to its band gap of 2.5 eV. Under visible-light irradiation, the electrons in valence bands (VB) of Al$_4$SiC$_4$ can be excited to the conduction bands (CB) (Eq. (2)). At the same time, the same number of holes is produced in the VB. The e^- and h^+ can transfer

to the surface of Al$_4$SiC$_4$ particles. Besides, RhB molecules could also be excited to form excited states (RhB*) by visible light due to photosensitization (Eq. (3)) [38]. The redox potentials of RhB and excited RhB* are 0.95 V and −1.42 V vs. NHE [63], respectively. It is much easier for RhB to be oxidized at its excited state. As the CB of Al$_4$SiC$_4$ is more positive than the redox potential of RhB*/RhB$^+$, electron transfers from RhB* to CB of Al$_4$SiC$_4$ and RhB molecules become RhB$^+$ (Eq. (4)), which leads the oxidation to further occur by h^+ (Eq. (5)). Since the VB (E_{VB} = + 1.1 eV vs. NHE) is less positive than the oxidation potential of OH$^-$/˙OH (E^0 = + 2.31 eV vs. NHE) [64] as shown in Fig. 11a, the OH$^-$ (H$_2$O) can't be oxidized to ˙OH by h^+, which is in good agreement with the result of scavenger experiments. The rGO performed as an electron acceptor to restrain the recombination of photo-induced electron-hole pair when Al$_4$SiC$_4$ particles were attached on the rGO sheets [65] as shown in Eq. (6). It has been reported that the work function of rGO is − 4.42 eV [66] and its redox potential vs. NHE is calculated to be − 0.08 V, which is much more positive than the CB of Al$_4$SiC$_4$. Therefore, the e^- can be easily transferred from the CB of Al$_4$SiC$_4$ to rGO. The redox potential of Cr(VI)/Cr(III) (E^0 = + 1.33 eV vs. NHE) [67] is much more positive than that of rGO. As a result, it is much easier for either the electron from CB of Al$_4$SiC$_4$ or from rGO to reduce Cr(VI) to Cr(III) (Eq. (7)). As mentioned above, the possible reaction processes for simultaneous reduction of Cr(VI) and oxidation of RhB is give in Eqs. (2)–(7):

$$Al_4SiC_4 + h\nu \rightarrow Al_4SiC_4(h^+) + Al_4SiC_4(e^-) \tag{2}$$

$$RhB + h\nu \rightarrow RhB* \tag{3}$$

$$RhB* + Al_4SiC_4 \rightarrow RhB^+ + Al_4SiC_4(e^-) \tag{4}$$

$$h^+ + RhB^+ \rightarrow CO_2 + H_2O + \text{mineral salts} \tag{5}$$

$$Al_4SiC_4(e^-) + rGO \rightarrow Al_4SiC_4 + rGO(e^-) \tag{6}$$

$$Cr_2O_7^{2-} + 14H^+ + 6e^- \rightarrow 2Cr^{3+} + 7H_2O \tag{7}$$

4. Conclusion

Novel Al$_4$SiC$_4$/rGO hybrids with a uniform dispersion Al$_4$SiC$_4$ particles on the surface of rGO sheets (2.5 mass%) were prepared by carbothermic reduction and hydrothermal method. The hybrid shows
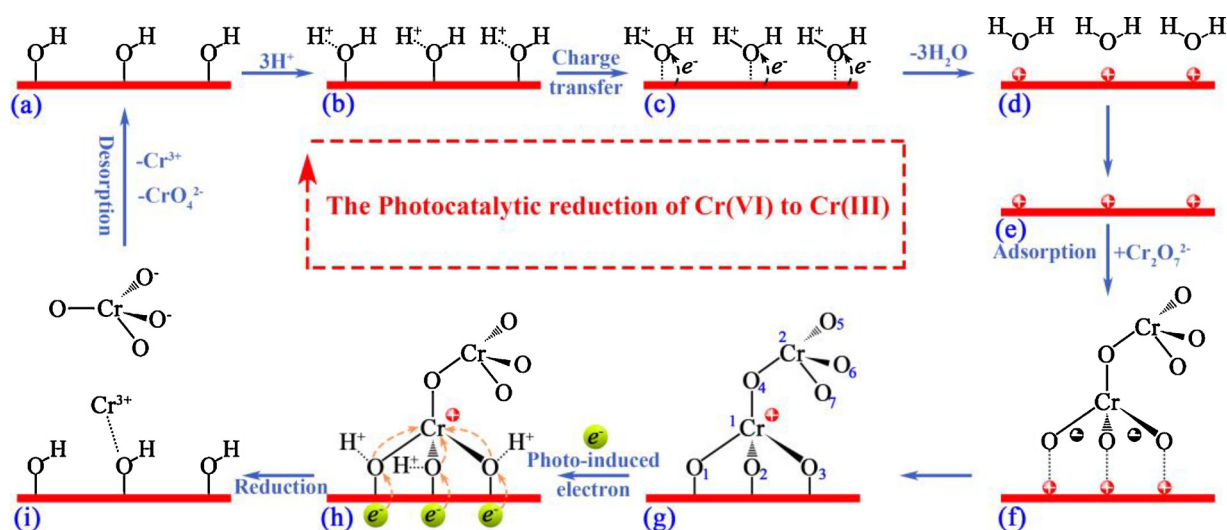

Fig. 8. Illustration of the dissociation of hydroxyls, the adsorption and reduction of Cr(VI) as well as the desorption of Cr(III) on the surface of Al$_4$SiC$_4$. (a) The Al$_4$SiC$_4$ surface with −OH adsorbed. (b) The Al$_4$SiC$_4$ surface with −OH$_2{}^+$ adsorbed. (c) The transfer of electrons from Al$_4$SiC$_4$ surface to −OH$_2{}^+$ groups. (d) The dissociation of hydroxyls in the form of neutral H$_2$O molecules. (e) Clear Al$_4$SiC$_4$ surface with positive charges. (f) The Al$_4$SiC$_4$ surface with Cr$_2$O$_7^{2-}$ ion adsorbed. (g) The Al$_4$SiC$_4$ surface with Cr$_2$O$_7^{2-}$ ion adsorbed after Charge redistribution. (h) The reduction of Cr(VI) to Cr(III). (i) The desorption of CrO$_4^{2-}$ and Cr(III). The thick red line represents the Al$_4$SiC$_4$ surface. To distinguish different O or Cr atoms, serial numbers are labeled next to the atoms in (g) (For interpretation of the references to colour in this figure legend, the reader is referred to the web version of this article).
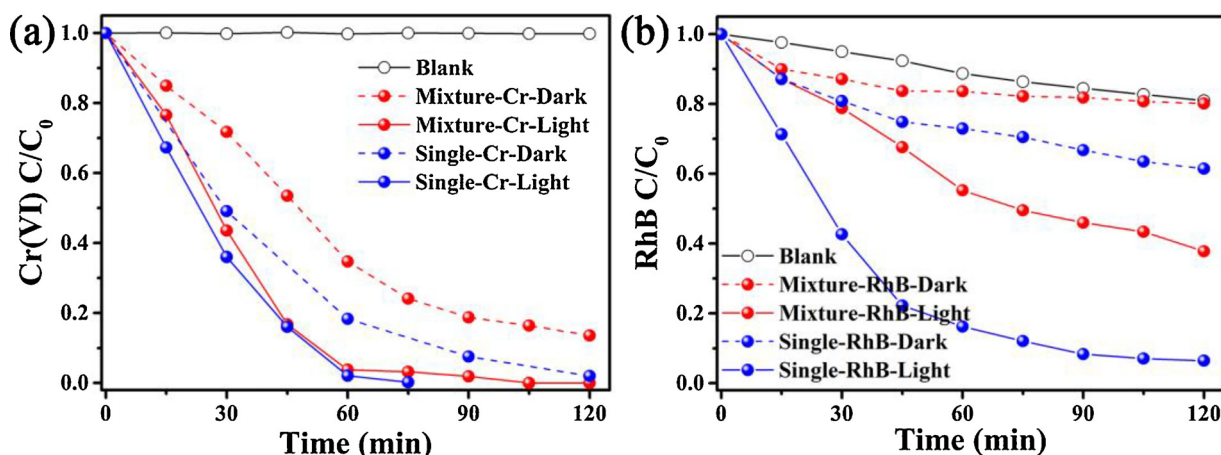
Fig. 9. Removal of (a) Cr(VI) or (b) RhB in single or mixture solution over Al_4SiC_4/rGO (2.5 mass%) photocatalyst in the dark or under irradiation.

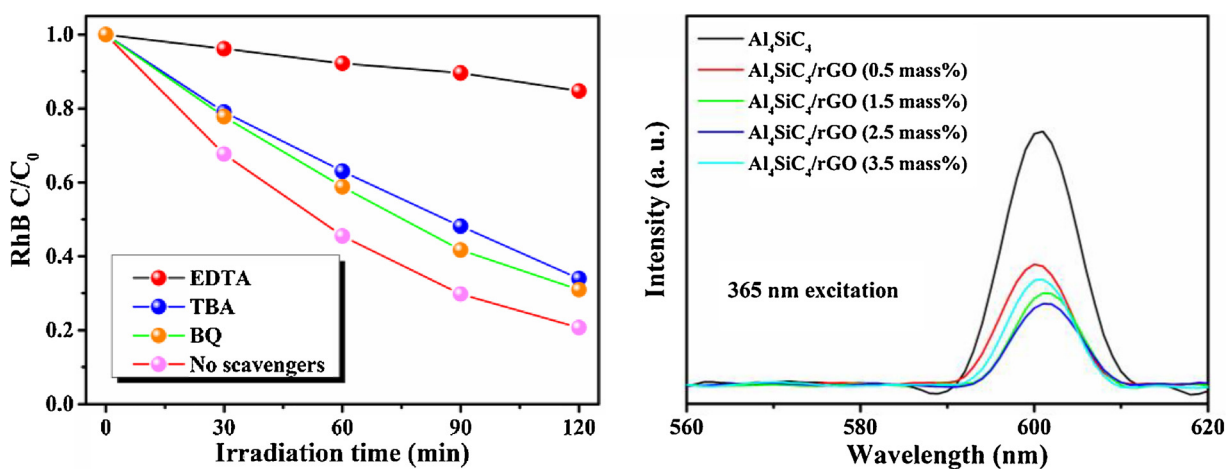**Fig. 10.** (a) Photocatalytic activity of Al_4SiC_4/rGO (2.5 mass%) for the degradation of RhB in the presence of different scavengers (catalyst dosage: 0.7 g/L, C_{RhB}: 10 mg/L, pH = 3.0, 100 mW/cm^2). (b) Photo-luminescence spectra for Al_4SiC_4 hybrids with different rGO contents.
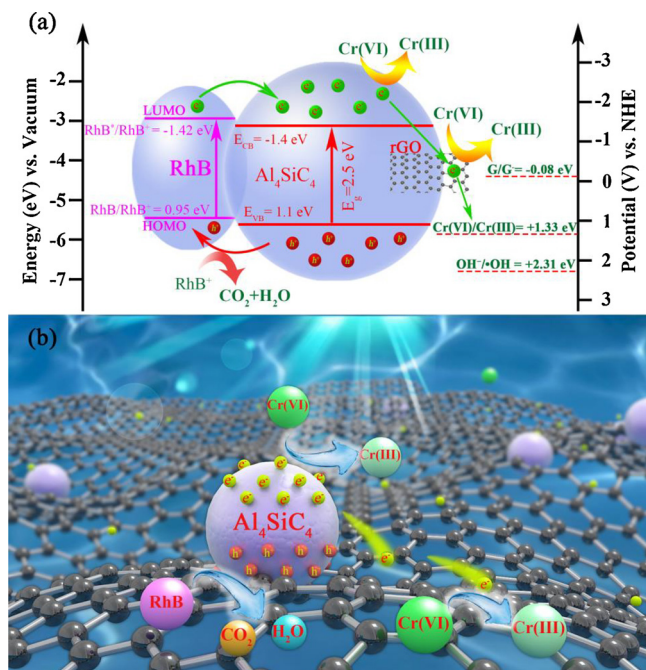

Fig. 11. (a) Energy diagram and (b) structural schematic illustration of Al_4SiC_4/rGO hybrids.

outstanding photocatalytic performance for simultaneous Cr(VI) reduction and RhB oxidation under visible light irradiation. The results show that the photocatalytic ratio of Cr(VI) and RhB is 96% and 45% after irradiation for 1 h. The high removal efficiency is attributed to two aspects. On the one hand, hydroxyl groups on Al_4SiC_4 can adsorb H^+ from the acidic solution, forming positive charges on Al_4SiC_4. These charges can greatly improve adsorption capacity of Cr(VI) anion and RhB. On the other hand, the addition of rGO increases the transfer of e^- and the separation rate of e^- and h^+. The resulting e^- and h^+ as main active species significantly contributes to the removal of Cr(VI) and RhB, respectively. Therefore, Al_4SiC_4 based hybrids are promising photocatalyst for the treatment of wastewater containing Cr(VI) and dyes.

Competing interests

The authors declare that they have no competing financial interests.

Acknowledgements

Appendix A. Supplementary data

Supplementary material related to this article can be found, in the online version, at doi:https://doi.org/10.1016/j.apcatb.2018.09.074.

References

[1] C.C. Wang, X.D. Du, J. Li, X.X. Guo, P. Wang, J. Zhang, Photocatalytic Cr(VI) reduction in metal-organic frameworks: a mini-review, Appl. Catal. B 193 (2016) 198–216.

[2] C.C. Wang, J.R. Li, X.L. Lv, Y.Q. Zhang, G. Guo, Photocatalytic organic pollutants degradation in metal–organic frameworks, Energy Environ. Sci. 7 (2014) 2831–2867.

[3] E.M. Dias, C. Petit, Towards the use of metal–organic frameworks for water reuse: a review of the recent advances in the field of organic pollutants removal and degradation and the next steps in the field, J. Mater. Chem. A 3 (2015) 22484–22506.

[4] N. Patel, R. Jaiswal, T. Warang, G. Scarduelli, A. Dashora, B.L. Ahuja, D.C. Kothari, A. Miotello, Efficient photocatalytic degradation of organic water pollutants using V–N-codoped TiO_2 thin films, Appl. Catal. B 150-151 (2014) 74–81.

[5] T. Karak, K. Bora, R.K. Paul, S. Das, P. Khare, A.K. Dutta, R.K. Boruah, Paradigm shift of contamination risk of six heavy metals in tea (Camellia sinensis L.) growing soil: A new approach influenced by inorganic and organic amendments, J. Hazard. Mater. 338 (2017) 250–264.

[6] A. Zhitkovich, Chromium in drinking water: sources, metabolism, and cancer risks, Chem. Res. Toxicol. 24 (2011) 1617–1629.

[7] J. Preethi, M.H. Farzana, S. Meenakshi, Photo-reduction of Cr(VI) using chitosan supported zinc oxide materials, Int. J. Biol. Macromol. 104 (2017) 1783–1793.

[8] M.V. Dozzi, S. Marzorati, M. Longhi, M. Coduri, L. Artiglia, E. Selli, Photocatalytic activity of TiO_2-WO_3 mixed oxides in relation to electron transfer efficiency, Appl. Catal. B 186 (2016) 157–165.

[9] H. Yu, S. Chen, X. Quan, H. Zhao, Y. Zhang, Fabrication of a TiO_2−BDD heterojunction and its application as a photocatalyst for the simultaneous oxidation of an azo dye and reduction of Cr(VI), Environ. Sci. Technol. 42 (2008) 3791–3796.

[10] Q. Wang, X. Chen, K. Yu, Y. Zhang, Y. Cong, Synergistic photosensitized removal of Cr(VI) and rhodamine B dye on amorphous TiO_2 under visible light irradiation, J. Hazard. Mater. 246-247 (2013) 135–144.

[11] Z. Jin, Y.X. Zhang, F.L. Meng, Y. Jia, T. Luo, X.Y. Yu, J. Wang, J.H. Liu, X.J. Huang, Facile synthesis of porous single crystalline ZnO nanoplates and their application in photocatalytic reduction of Cr(VI) in the presence of phenol, J. Hazard. Mater. 276 (2014) 400–407.

[12] Y. Li, Y. Bian, H. Qin, Y. Zhang, Z. Bian, Photocatalytic reduction behavior of hexavalent chromium on hydroxyl modified titanium dioxide, Appl. Catal. B 206 (2017) 293–299.

[13] L. Pedesseau, J. Even, M. Modreanu, D. Chaussende, E. Sarigiannidou, O. Chaix-Pluchery, O. Durand, Al_4SiC_4 wurtzite crystal: Structural, optoelectronic, elastic, and piezoelectric properties, APL Mater. 3 (2015) 121101.

[14] D. Zevgitis, O. Chaix-Pluchery, B. Doisneau, M. Modreanu, J. La Manna, E. Sarigiannidou, D. Chaussende, Synthesis and characterization of Al_4SiC_4: a "new" wide band gap semiconductor material, Mater. Sci. Forum 821–823 (2015) 974–977.

[15] J. Chen, Z. Zhang, W. Mi, E. Wang, B. Li, K.C. Chou, X. Hou, Fabrication and oxidation behavior of Al_4SiC_4 powders, J. Am. Ceram. Soc. 100 (2017) 3145–3154.

[16] Y.L. Wu, F. Bai, T. Yang, J.H. Chen, L. Su, X.M. Hou, Selective determination of copper (II) based on aluminum silicon carbide nanoparticles modified glassy carbon electrode by square wave stripping voltammetry, Electroanalysis 29 (2017) 2224–2231.

[17] Y. Wu, T. Yang, K.C. Chou, J. Chen, L. Su, X. Hou, The effective determination of Cd (ii) and Pb(ii) simultaneously based on an aluminum silicon carbide-reduced graphene oxide nanocomposite electrode, Analyst 142 (2017) 2741–2747.

[18] K. Chang, Z. Mei, T. Wang, Q. Kang, S. Ouyang, J. Ye, MoS_2/graphene cocatalyst for efficient photocatalytic H_2 evolution under visible light irradiation, ACS Nano 8 (2014) 7078–7087.

[19] B. Qiu, M. Xing, J. Zhang, Mesoporous TiO_2 nanocrystals grown in situ on graphene aerogels for high photocatalysis and lithium-ion batteries, J. Am. Chem. Soc. 136 (2014) 5852–5855.

[20] B. Chen, E. Liu, T. Cao, F. He, C. Shi, C. He, L. Ma, Q. Li, J. Li, N. Zhao, Controllable graphene incorporation and defect engineering in MoS_2-TiO_2 based composites: towards high-performance lithium-ion batteries anode materials, Nano Energy 33 (2017) 247–256.

[21] Y. Lu, X. Cheng, G. Tian, H. Zhao, L. He, J. Hu, S.-M. Wu, Y. Dong, G.-G. Chang, S. Lenaerts, S. Siffert, G. Van Tendeloo, Z.-F. Li, L.-L. Xu, X.-Y. Yang, B.-L. Su, Hierarchical CdS/m-TiO_2/G ternary photocatalyst for highly active visible light-induced hydrogen production from water splitting with high stability, Nano Energy 47 (2018) 8–17.

[22] Z.J. Fan, W. Kai, J. Yan, T. Wei, L.J. Zhi, J. Feng, Y.M. Ren, L.P. Song, F. Wei, Facile synthesis of graphene nanosheets via Fe reduction of exfoliated graphite oxide, ACS Nano 5 (2011) 191–198.

[23] A.E. Nogueira, O.F. Lopes, A.B.S. Neto, C. Ribeiro, Enhanced Cr(VI) photoreduction in aqueous solution using Nb_2O_5/CuO heterostructures under UV and visible irradiation, Chem. Eng. J. 312 (2017) 220–227.

[24] X. Liu, L. Pan, T. Lv, G. Zhu, Z. Sun, C. Sun, Microwave-assisted synthesis of CdS-reduced graphene oxide composites for photocatalytic reduction of Cr(VI), Chem. Commun. 47 (2011) 11984–11986.

[25] X. Liu, L. Pan, Q. Zhao, T. Lv, G. Zhu, T. Chen, T. Lu, Z. Sun, C. Sun, UV-assisted photocatalytic synthesis of ZnO–reduced graphene oxide composites with enhanced photocatalytic activity in reduction of Cr(VI), Chem. Eng. J. 183 (2012) 238–243.

[26] Y.F. Sun, W.K. Chen, W.J. Li, T.J. Jiang, J.H. Liu, Z.G. Liu, Selective detection toward Cd^{2+} using Fe_3O_4/RGO nanoparticle modified glassy carbon electrode, J. Electroanal. Chem. 714–715 (2014) 97–102.

[27] X. Huang, G. Wen, Reaction synthesis of aluminum silicon carbide ceramics, Mater. Chem. Phys. 97 (2006) 193–199.

[28] Y. Ping, J.M. Yan, Z.L. Wang, H.L. Wang, Q. Jiang, $Ag_{0.1}$-$Pd_{0.9}$/rGO: an efficient catalyst for hydrogen generation from formic acid/sodium formate, J. Mater. Chem. A 1 (2013) 12188.

[29] B.J. Tan, L. Hwan, S.L. Suib, F.S. Galasso, Spectroscopic characterization of CVD Ti coating on SiC-coated boron fibers, Chem. Mater. 3 (1991) 368–378.

[30] I. Iatsunskyi, M. Kempiński, M. Jancelewicz, K. Załęski, S. Jurga, V. Smyntyna, Structural and XPS characterization of ALD Al_2O_3 coated porous silicon, Vacuum 113 (2015) 52–58.

[31] J. Wang, G. Zhang, P. Zhang, Layered birnessite-type MnO_2 with surface pits for enhanced catalytic formaldehyde oxidation activity, J. Mater. Chem. A 5 (2017) 5719–5725.

[32] Y. Kang, L. Wang, Y. Wang, H. Zhang, Y. Wang, D. Hong, Y. Qv, S. Wang, Construction and enhanced gas sensing performances of CuO-modified α-Fe_2O_3 hybrid hollow spheres, Sens. Actuators B 177 (2013) 570–576.

[33] D. Tang, G. Zhang, Fabrication of $AgFeO_2$/g-C_3N_4 nanocatalyst with enhanced and stable photocatalytic performance, Appl. Surf. Sci. 391 (2017) 415–422.

[34] T. Xu, L. Zhang, H. Cheng, Y. Zhu, Significantly enhanced photocatalytic performance of ZnO via graphene hybridization and the mechanism study, Appl. Catal. B 101 (2011) 382–387.

[35] D. Hou, X. Hu, Y. Wen, B. Shan, P. Hu, X. Xiong, Y. Qiao, Y. Huang, Electrospun sillenite $Bi_{12}MO_{20}$ (M = Ti, Ge, Si) nanofibers: general synthesis, band structure, and photocatalytic activity, Phys. Chem. Chem. Phys. 15 (2013) 20698–20705.

[36] Z. Wan, G. Zhang, X. Wu, S. Yin, Novel visible-light-driven Z-scheme $Bi_{12}GeO_{20}$/g-C_3N_4 photocatalyst: oxygen-induced pathway of organic pollutants degradation and proton assisted electron transfer mechanism of Cr(VI) reduction, Appl. Catal. B 207 (2017) 17–26.

[37] Z. Xiong, L.L. Zhang, J. Ma, X.S. Zhao, Photocatalytic degradation of dyes over graphene-gold nanocomposites under visible light irradiation, Chem. Commun. 46 (2010) 6099–6101.

[38] M. Wang, L. Sun, Z. Lin, J. Cai, K. Xie, C. Lin, P–n Heterojunction photoelectrodes composed of Cu_2O-loaded TiO_2 nanotube arrays with enhanced photoelectrochemical and photoelectrocatalytic activities, Energy Environ. Sci. 6 (2013) 1211.

[39] T. Yang, W. Liu, L. Li, J. Chen, X. Hou, K.C. Chou, Synergizing the multiple plasmon resonance coupling and quantum effects to obtain enhanced SERS and PEC performance simultaneously on a noble metal-semiconductor substrate, Nanoscale 9 (2017) 2376–2384.

[40] F. Liu, J. Yu, G. Tu, L. Qu, J. Xiao, Y. Liu, L. Wang, J. Lei, J. Zhang, Carbon nitride coupled Ti-SBA15 catalyst for visible-light-driven photocatalytic reduction of Cr (VI) and the synergistic oxidation of phenol, Appl. Catal. B 201 (2017) 1–11.

[41] Y. Li, W. Cui, L. Liu, R. Zong, W. Yao, Y. Liang, Y. Zhu, Removal of Cr(VI) by 3D TiO_2-graphene hydrogel via adsorption enriched with photocatalytic reduction, Appl. Catal. B 199 (2016) 412–423.

[42] Q. Sun, X. Hu, S. Zheng, Z. Sun, S. Liu, H. Li, Influence of calcination temperature on the structural, adsorption and photocatalytic properties of TiO_2 nanoparticles supported on natural zeolite, Powder Technol. 274 (2015) 88–97.

[43] Q. Sun, H. Li, S. Zheng, Z. Sun, Characterizations of nano-TiO_2/diatomite composites and their photocatalytic reduction of aqueous Cr(VI), Appl. Surf. Sci. 311 (2014) 369–376.

[44] Y. Zhang, Z. Chen, S. Liu, Y. Xu, Size effect induced activity enhancement and anti-photocorrosion of reduced graphene oxide/ZnO composites for degradation of organic dyes and reduction of Cr(VI) in water, Appl. Catal. B 140–141 (2013) 598–607.

[45] H. Xu, Z. Wu, M. Ding, X. Gao, Microwave-assisted synthesis of flower-like BN/BiOCl composites for photocatalytic Cr(VI) reduction upon visible-light irradiation, Mater. Des. 114 (2017) 129–138.

[46] X. Liu, L. Pan, T. Lv, G. Zhu, T. Lu, Z. Sun, C. Sun, Microwave-assisted synthesis of TiO_2-reduced graphene oxide composites for the photocatalytic reduction of Cr(VI), RSC Adv. 1 (2011) 1245.

[47] J. Qu, D. Chen, N. Li, Q. Xu, H. Li, J. He, J. Lu, Coral-inspired nanoscale design of porous SnS_2 for photocatalytic reduction and removal of aqueous Cr (VI), Appl. Catal. B 207 (2017) 404–411.

[48] Y.C. Zhang, L. Yao, G. Zhang, D.D. Dionysiou, J. Li, X. Du, One-step hydrothermal synthesis of high-performance visible-light-driven SnS_2/SnO_2 nanoheterojunction photocatalyst for the reduction of aqueous Cr(VI), Appl. Catal. B 144 (2014) 730–738.

[49] M. Naimi-Joubani, M. Shirzad-Siboni, J.-K. Yang, M. Gholami, M. Farzadkia, Photocatalytic reduction of hexavalent chromium with illuminated ZnO/TiO_2 composite, J. Ind. Eng. Chem. 22 (2015) 317–323.

[50] E. Desimoni, C. Malitesta, P.G. Zambonin, J.C. Rivière, An x-ray photoelectron spectroscopic study of some chromium-oxygen systems, Surf. Interface Anal. 13 (1988) 173–179.

[51] W. Chen, T. Wang, J. Xue, S. Li, Z. Wang, S. Sun, Cobalt-nickel layered double hydroxides modified on TiO_2 nanotube arrays for highly efficient and stable PEC water splitting, Small 13 (2017) 1602420.

[52] Y. Zhang, M. Xu, H. Li, H. Ge, Z. Bian, The enhanced photoreduction of Cr(VI) to Cr (III) using carbon dots coupled TiO_2 mesocrystals, Appl. Catal. B 226 (2018) 213–219.

[53] W. Li, D. He, G. Hu, X. Li, G. Banerjee, J. Li, S.H. Lee, Q. Dong, T. Gao,

G.W. Brudvig, M.M. Waegele, D.E. Jiang, D. Wang, Selective CO production by photoelectrochemical methane oxidation on TiO_2, ACS Cent. Sci. 4 (2018) 631–637.

[54] R. Schlogl, Heterogeneous catalysis, Angew. Chem. Int. Ed. 54 (2015) 3465–3520.

[55] A. Corma, Heterogeneous catalysis: understanding for designing, and designing for applications, Angew. Chem. Int. Ed. 55 (2016) 6112–6113.

[56] S. Hu, X. Qu, P. Li, F. Wang, Q. Li, L. Song, Y. Zhao, X. Kang, Photocatalytic oxygen reduction to hydrogen peroxide over copper doped graphitic carbon nitride hollow microsphere: the effect of Cu(I)-N active sites, Chem. Eng. J. 334 (2018) 410–418.

[57] Z. Konvičková, V. Holišová, M. Kolenčík, T. Niide, G. Kratošová, M. Umetsu, J. Seidlerová, Phytosynthesis of colloidal Ag-AgCl nanoparticles mediated by Tilia sp. leachate, evaluation of their behaviour in liquid phase and catalytic properties, Colloid Polym. Sci. 296 (2018) 677–687.

[58] J. Zhao, T. Wu, K. Wu, K. Oikawa, H. Hidaka, N. Serpone, Photoassisted degradation of dye pollutants. 3. Degradation of the cationic dye rhodamine B in aqueous anionic surfactant/TiO_2 dispersions under visible light irradiation: evidence for the need of substrate adsorption on TiO_2 particles, Environ. Sci. Technol. 32 (1998) 2394–2400.

[59] H. Fida, S. Guo, G. Zhang, Preparation and characterization of bifunctional Ti-Fe kaolinite composite for Cr(VI) removal, J. Colloid Interface Sci. 442 (2015) 30–38.

[60] J. Su, L. Zhu, P. Geng, G. Chen, Self-assembly graphitic carbon nitride quantum dots anchored on TiO_2 nanotube arrays: an efficient heterojunction for pollutants degradation under solar light, J. Hazard. Mater. 316 (2016) 159–168.

[61] L. Hu, F. Chen, P. Hu, L. Zou, X. Hu, Hydrothermal synthesis of SnO_2/ZnS nanocomposite as a photocatalyst for degradation of Rhodamine B under simulated and natural sunlight, J. Mol. Catal. A Chem. 411 (2016) 203–213.

[62] P. Zhang, T. Song, T. Wang, H. Zeng, In-situ synthesis of Cu nanoparticles hybridized with carbon quantum dots as a broad spectrum photocatalyst for improvement of photocatalytic H_2 evolution, Appl. Catal. B 206 (2017) 328–335.

[63] J. He, J. Wang, Y. Chen, J. Zhang, D. Duan, Y. Wang, Z. Yan, A dye-sensitized Pt@UiO-66(Zr) metal-organic framework for visible-light photocatalytic hydrogen production, Chem. Commun. 50 (2014) 7063–7066.

[64] X. Li, T. Wan, J. Qiu, H. Wei, F. Qin, Y. Wang, Y. Liao, Z. Huang, X. Tan, In-situ photocalorimetry-fluorescence spectroscopy studies of RhB photocatalysis over Z-scheme g-C_3N_4@Ag@Ag_3PO_4 nanocomposites: a pseudo-zero-order rather than a first-order process, Appl. Catal. B 217 (2017) 591–602.

[65] X. Meng, Z. Zhang, Bi_2MoO_6 co-modified by reduced graphene oxide and palladium (Pd^{2+} and Pd°) with enhanced photocatalytic decomposition of phenol, Appl. Catal. B 209 (2017) 383–393.

[66] N. Yang, J. Zhai, D. Wang, Y. Chen, L. Jiang, Two-dimensional graphene bridges enhanced photoinduced charge transport in dye-sensitized solar cells, ACS Nano 4 (2010) 887–894.

[67] Q. Yuan, L. Chen, M. Xiong, J. He, S.L. Luo, C.T. Au, S.F. Yin, Cu_2O/$BiVO_4$ heterostructures: Synthesis and application in simultaneous photocatalytic oxidation of organic dyes and reduction of Cr(VI) under visible light, Chem. Eng. J. 255 (2014) 394–402.